Journal of Biomedical Optics

BiomedicalOptics.SPIEDigitalLibrary.org

Contrast-enhanced photoacoustic imaging in the second near-infrared window using semiconducting polymer nanoparticles

Paul Kumar Upputuri
Cangjie Yang
Shuo Huang
Kai Wang
Mingfeng Wang
Manojit Pramanik

SPIE.

Paul Kumar Upputuri, Cangjie Yang, Shuo Huang, Kai Wang, Mingfeng Wang, Manojit Pramanik, "Contrast-enhanced photoacoustic imaging in the second near-infrared window using semiconducting polymer nanoparticles," *J. Biomed. Opt.* **24**(3), 031002 (2019), doi: 10.1117/1.JBO.24.3.031002.

Journal of Biomedical Optics 24(3), 031002 (March 2019)

Contrast-enhanced photoacoustic imaging in the second near-infrared window using semiconducting polymer nanoparticles

Paul Kumar Upputuri, Cangjie Yang, Shuo Huang, Kai Wang, Mingfeng Wang,* and Manojit Pramanik*
Nanyang Technological University, School of Chemical and Biomedical Engineering, Singapore

Abstract. Photoacoustic imaging (PAI) is a fast growing deep-tissue imaging modality. However, light scattering and absorption in biological tissues limit imaging depth. Short near-infrared wavelengths (650 to 950 nm) are widely used for PAI. Using longer near-infrared wavelengths reduces scattering. We demonstrate deep-tissue contrast-enhanced *in vivo* photoacoustic imaging at a wavelength of 1064 nm. An ultranarrow bandgap semiconducting polymer poly (thienoisoindigo-alt-diketopyrrolopyrrole) (denoted as PIGD) is designed and demonstrated for imaging at 1064 nm. By embedding colloidal nanoparticles (NPs) of PIGD in chicken-breast tissue, an imaging depth of ~5 cm is achieved. Intravenous injection of PIGD NPs in living rats showed brain vascular images with ~2 times higher contrast compared with the brain vascular images without any contrast agent. Thus, PIGD NPs as an NIR-II contrast agent opens new opportunities for both preclinical and clinical imaging of deep tissues with enhanced contrast. [DOI: 10.1117/1.JBO.24.3.031002]

Keywords: photoacoustic tomography; second near-infrared window; deep-tissue imaging; brain vascular imaging; biomaterials.

Paper 180108SSR received Feb. 19, 2018; accepted for publication May 21, 2018; published online Aug. 17, 2018.

1 Introduction

Photoacoustic tomography (PAT) is an emerging hybrid imaging modality that has found many demanding applications in both clinical and preclinical studies.[1–5] PAT combines high optical contrast and scalable ultrasound resolution in a single modality. In PAT, short (nanosecond) laser pulses are absorbed by tissue chromophores and converted to transient heating, which is subsequently converted into an acoustic wave due to thermo-elastic expansion. Images are formed by reconstructing the PA signals acquired at various positions around the tissue surface. Conventional PAT systems use Nd:YAG-pumped optical parametric oscillator (OPO) laser as PA excitation source. Nd:YAG lasers typically emit light with a wavelength of 1064 nm, which is then frequency-doubled to obtain 532 nm. The OPO pumped by 532 nm can generate light wavelengths ranging from 650 to 950 nm (NIR-I window). Due to the reduced scattering in biological tissues, NIR-I window is widely used for deep-tissue PA imaging.[6,7] Several contrast agents based on metallic, inorganic, organic nanoparticles, quantum dots, carbon nanotubes, etc., were used for NIR-I window imaging.[8–10] Contrast agents are useful for enhancing the image contrast, for targeted molecular imaging, drug delivery, therapy, etc.[11–13]

Recent studies on optical imaging have found that NIR-II window (1000 to 1700 nm) can provide quality imaging compared with NIR-I window.[14,15] The fundamental of Nd:YAG laser is 1064 nm, it belongs to the NIR-II window. The advantages of using 1064 nm for PA imaging include: (i) according to the ANSI safety limit, the maximum permissible exposure (MPE) for skin is 100 mJ/cm^2 at 1064 nm, whereas it is ~30 mJ/cm^2 at 800 nm.[16] So, more energy can be used at 1064 nm, which may contribute to deeper imaging. (ii) 1064-nm Nd:YAG ns-laser is cheaper and more compact compared with the OPO lasers (or dye laser) required for NIR-I window imaging. However, at NIR-II wavelengths the absorption from endogenous contrast agents (blood, lipid, etc.) is relatively low. Thus, there is a need for NIR-II contrast agents. The NIR-II contrast agents reported so far are copper sulfide (CuS) nanoparticles,[17] silver (Ag) nanoplates,[18] gold (Au) nanorods,[19] phosphorous phthalocyanine (P-Pc),[20] and hyperbranched Au plasmonic blackbody (AuPB).[21] In particular, semiconducting polymer nanoparticles (SPNs), composed of macromolecular chromophores with strong light absorption and robust photostability, have appeared as a new generation of PA contrast agent in the NIR-II-region.[22–24] These SPNs as PA contrast agents have demonstrated enhanced photostability and good biocompatibility compared with inorganic NPs and small molecular chromophores in imaging of living mice.[8,25–29] The studies in photoacoustic imaging proved that NIR-II wavelengths can provide better imaging depth compared with NIR-I wavelengths. An increase in the imaging depth is due to reduced tissue scattering at a longer wavelength. Moreover, at 1064-nm wavelengths more excitation energy ~100 mJ/cm can be used for imaging, as a result more light can reach deeper compared with the NIR-I window that allows only ~30 mJ/cm^2 at 800 nm. This promising behavior motivated us to explore other semiconducting polymers with high absorption coefficient in the NIR-II region.

Herein, we present a new kind of NIR-II absorbing SPNs composed of ultranarrow bandgap (refers to the optical bandgap of the polymer) semiconducting polymers poly (thienoisoindigo-alt-diketopyrrolepyrrole) (denoted as PIGD, Fig. 1) for PA imaging in the NIR-II window. Both thienoisoindigo (TIIG) and diketopyrrolopyrrole (DPP) have been employed as building blocks to

*Address all correspondence to: Mingfeng Wang, E-mail: mfwang@ntu.edu.sg; Manojit Pramanik, E-mail: manojit@ntu.edu.sg

construct a myriad of narrow bandgap semiconducting polymers owing to their high structural planarity.[30–32] Most of them have shown outstanding performances in organic electronic devices, such as polymer solar cells[33,34] and field-effect transistors.[35,36] Very recently, we combined these two building blocks to construct a new semiconducting polymer PIGD, giving average molecular weight of 24.0 kDa and an optical bandgap as narrow as 0.8 eV.[37] The lower the optical bandgap of the SNPs, the longer wavelength of the light absorption by the SNPs. As a consequence, the deeper tissue-penetration depth is expected, which benefits PA imaging. Despite the synthetic chemistry of PIGD has been reported, the processing of PIGD into colloidal nanoparticles in water, the characterization of the nanoparticles, and their application for the second near-infrared window photoacoustic imaging have not been reported. These properties inspired us to explore their application in PA imaging in the NIR-II window.

In this work, we present a Q-switched Nd:YAG 1064-nm laser-based photoacoustic tomography system for NIR-II window imaging. The design and synthesis of the PIGD NPs that has strong absorption in NIR-II window are presented. The optical and PA properties of the PIGD NPs are discussed. Then, to validate the photoacoustic imaging capabilities of PIGD NPs, we performed deep-tissue imaging experiments at 1064-nm wavelength. At last, the proof-of-concept application of PIGD NPs for NIR-II window PA imaging is demonstrated by imaging brain vasculatures in living rats.

2 Materials and Methods

2.1 *Materials*

10 × phosphate buffer saline (PBS) buffer with pH = 7.4 (ultrapure grade) is a commercial product of first BASE Singapore. MilliQ water (18.2 MQ) was used to prepare the

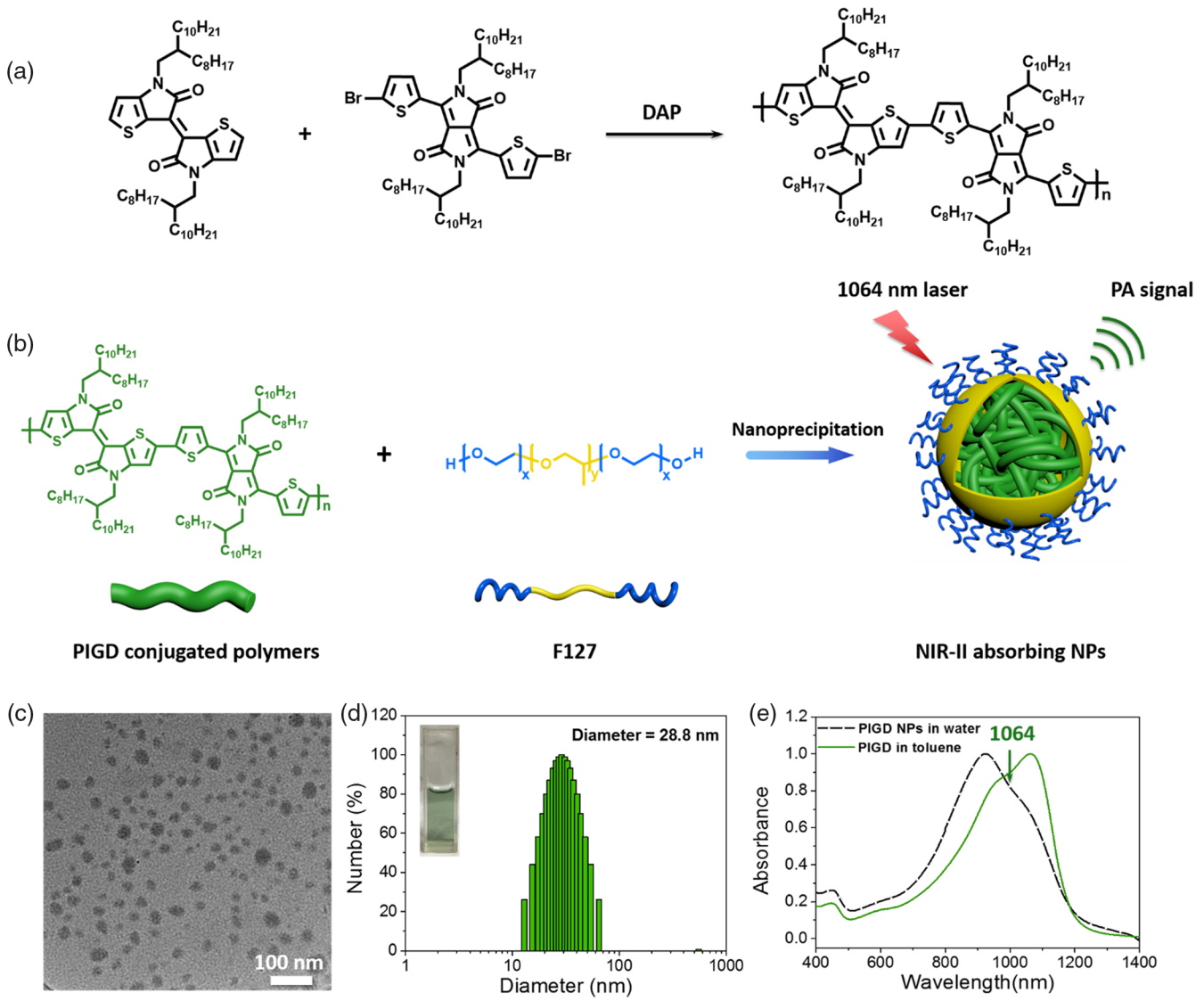

Fig. 1 (a) Synthesis of conjugated polymer PIGD by direct arylation polymerization, (b) schematic illustration of conjugated PIGD encapsulated by surfactant F127 upon nanoprecipitation in water/THF mixture followed by evaporation of THF, resulting in colloidal nanoparticles with PIGD as the core, PPO as the shell and PEO as the corona, (c) TEM image of air-dried PIGD NPs in water, (d) DLS result of PIGD NPs in water; the inset of (d) is the digit photo of PIGD NPs dispersion under room light, and (e) UV-vis-NIR absorption spectra of PIGD in water.

buffer solution from the 10 × PBS stock buffer. 1 × PBS consists of NaCl (137 mM), KCl (2.7 mM), Na_2HPO_4 (10 mM), and KH_2PO_4 (1.8 mM). Chloroform-D (99%) was purchased from Cambridge Isotope Laboratories, Inc. All other chemicals and reagents were purchased from Aldrich or Merck and used as received unless otherwise specified. Conjugated polymer PIGD was synthesized according to our previous report.

2.2 *Characterization*

UV–vis-NIR absorption spectra of the samples were measured on a SHIMADZU UV-2450 spectrophotometer. TEM measurements were performed with a TEM Carl Zeiss Libra 120 Plus at an acceleration voltage of 120 kV. A 5-μL droplet of diluted samples was directly dropped onto a copper grid (300 mesh) coated with a carbon film, followed by drying at room temperature. The size distribution of resulting nanoparticles was determined by dynamic light scattering (DLS) using a BI-200SM (Brookhaven) with angle detection at 90 deg.

2.3 *Preparation of Nanoparticles*

Conjugated polymer PIGD (5 mg) and macromolecular surfactant Pluronic F-127 (50 mg) were co-dissolved in 0.5 mL of THF. The mixture was rapidly injected into 2.5 mL of 1 × PBS buffer under ultrasonication (Alstron ultrasonic cleaner, model: ALD-40100-38H). After evaporation of excess THF, a well-dispersed solution of PIGD NPs with a concentration of 2 mg/mL was obtained. Specifically, a mixture of PIGD polymers and a macromolecular surfactant Pluronic F-127 (The mass ratio of PIGD and F127 is 1 : 10) codissolved in 1 mL of THF was rapidly injected into 10 mL of water under sonication [Fig. 1(b)], followed by exposure in air at room temperature overnight to remove THF. The resulting SPNs were well-dispersed in PBS buffer.

2.4 *PAT System for Imaging at 1064-nm Wavelength*

A home-made PAT system was used for PA measurements. The excitation source is 1064 nm Nd:YAG laser (Continuum, Surelite Ex) that can generate 5-ns pulses at 10-Hz repetition rate. The 1064-nm beam was guided to the circular scanner, and homogenized using an optical ground glass (GG). The test sample and the ultrasound transducer (UST) were immersed in water for coupling the PA signal to the transducer. The PA signal generated by the sample was received by a nonfocused transducer (V323-SU/2.25 MHz, Olympus NDT) with a 13-mm active area and 70% nominal bandwidth. The PA signals were subsequently amplified, bandpass filtered by an ultrasound pulser/receiver unit (AU), (Olympus NDT, 5072PR), and then digitized and recorded by the PC with a DAQ (data acquisition) card (25 Ms/s, GaGe, compuscope 4227). For solution-level testing, we performed experiments on fresh rat blood and PIGD NPs inside a low-density polyethylene tube [inner diameter (ID) = 0.59 mm, outer diameter (OD) = 0.78 mm]. For two-dimensional (2-D) imaging, the transducer was driven by a computer-controlled stepper motor (SM) to continuously move in a circular motion. The acquired A-lines were used to reconstruct the PA image of the sample using a delay-and-sum back projection algorithm.[38,39] The imaging system has a spatial resolution of ~380 μm using 2.25-MHz UST.

2.5 *Agar Gel Phantom for Deep-Tissue Imaging*

To demonstrate the deep-tissue imaging capability of the system, three agar gel cylinders containing PIGD NPs with different concentrations were embedded inside agar gel of 2.5 cm in diameter. The three cylinders s1, s2, and s3 [Fig. 3(a)] contain PIGD NPs with concentrations 1.0, 0.5, and 0.25 mg/mL, respectively. Fresh chicken-breast tissue slices were cut and placed on the phantom to determine the maximum imaging depth. The chicken slice fully covered the phantom to avoid leakage of light to the sample. Several slices of chicken-breast tissue were sequentially placed to make the objects at different depths from the laser-illuminated tissue surface.

2.6 *Imaging Rat Brain Vasculature In Vivo*

For brain vascular imaging, NTac:Sprague Dawley®SD® healthy female rats of body weight ~95 ± 3 gm, procured from InVivos Pte. Ltd., Singapore, were used. All the *in vivo* experiments were performed according to the guidelines and regulations approved by the institutional Animal Care and Use committee of Nanyang Technological University, Singapore (Animal Protocol Number ARF-SBS/NIE-A0263). Before going for brain vascular imaging, the rat was anaesthetized for short period of time to depilate the hair on the scalp and to mount it inside the scanner. This anaesthesia mixture was prepared with 2 mL of Ketamine (100 mg/mL), 2 mL of xylazine (20 mg/mL), and 1 mL of saline. 0.2 mL per 100 g rat weight was injected intraperitoneally. This ketamine/xylazine cocktail can make the animal anesthetized for 30 to 40 min. For brain vascular imaging, the hair on the scalp was depilated. The animal was mounted in the system as shown in Fig. 2(a). While acquiring images in post-injection time period (about 2 h), the anaesthesia was achieved by the continuous inhalation of a mixture of 1.0 L/ min oxygen and 0.75% isoflurane. PAT imaging was performed before the injection of the contrast agent. Afterward, PIGD NPs (0.25 mL, 2 mg/mL) was injected into the rat tail vein, then PAT images were acquired for about 2 hours. After collecting the data, the animal was euthanized by the intraperitoneal injection of pentobarbital (300 mg/mL).

3 Results and Discussion

3.1 *Preparation and Characterization of NIR-II Light-Absorbing Polymeric Nanoparticles*

The synthesis of PIGD semiconducting polymers is described in Fig. 1(a). Direct arylation polymerization (DAP) was utilized to synthesize the target semiconducting polymers by coupling between the brominated DPP and nonbrominated TIIG monomers under our optimized reaction conditions.[40–42] In contrast to conventional cross-coupling techniques, such as Suzuki[43] coupling or Stille[44] coupling, which requires preactivation of C-H bonds, DAP technique enables the synthesis of semiconducting polymers in fewer steps. Moreover, the absence of flammable organometallic reagents and toxic byproducts makes DAP as a better choice to afford more synthetically scalable and biocompatible materials for biological applications.

PIGD SPNs were prepared by a traditional method of nanoprecipitation.[45,46] The representative transmission electron microscopy (TEM) image [Fig. 1(c)] shows that the PIGD SPNs appear spherical, with an average diameter of 21 ± 5 nm in the dry state, which is smaller than that (28.8 nm) in the hydrated state in water as measured with DLS [Fig. 1(d)]. This dispersion

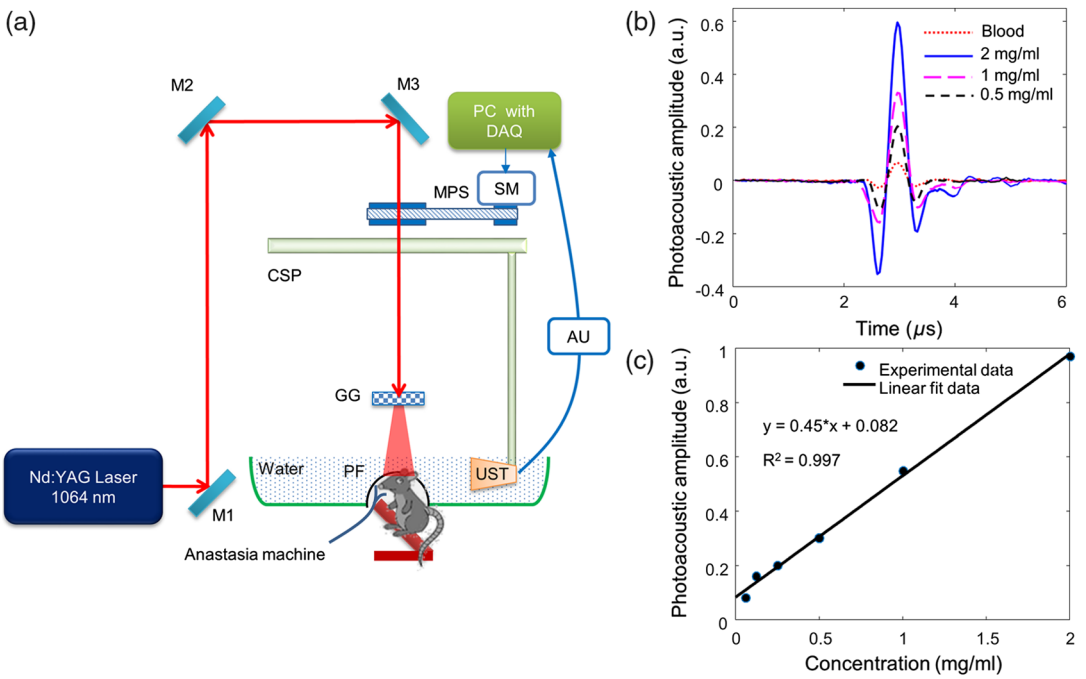

Fig. 2 (a) Schematic diagram of NIR-II PAT system. Here, M, mirror; CSP, circular scanning plate; MPS, motor pulley system, SM, stepper motor; DAQ, data acquisition card; AU, ultrasound pulser/receiver unit; UST, ultrasound transducer; GG, ground glass; PF, 100-μm transparent polythene membrane; (b) PA signals of PIGD NPs compared with fresh rat blood, and (c) PA amplitude as a function of concentration of PIGD nanoparticles.

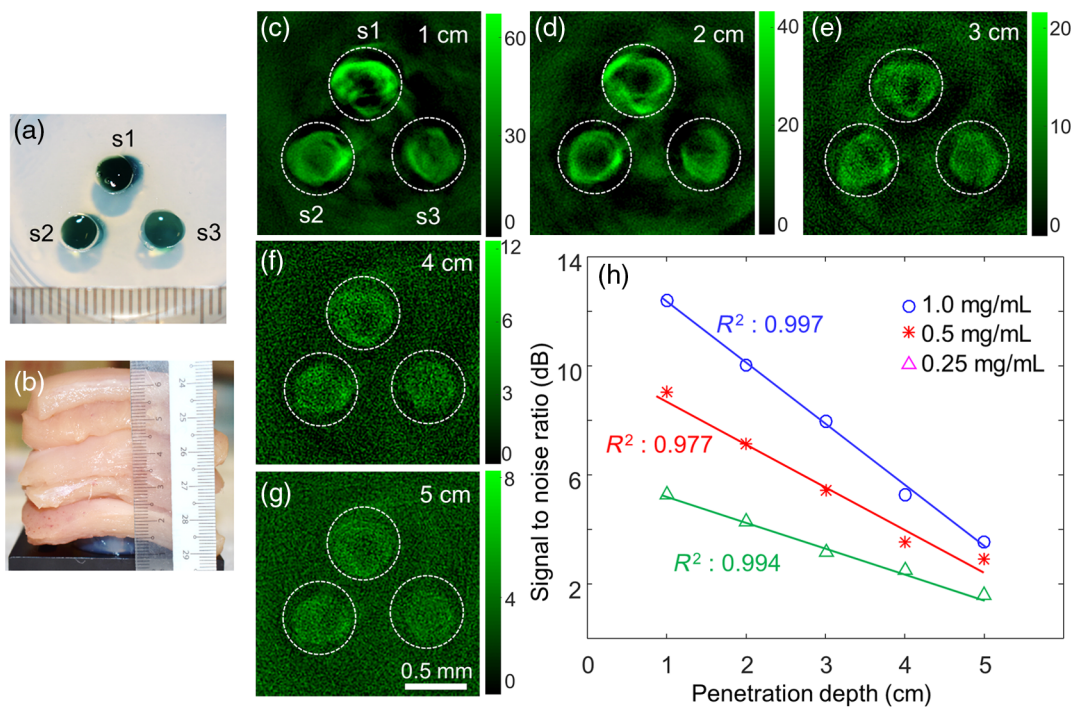

Fig. 3 Deep-tissue PA imaging of PIGD NPs embedded inside chicken-breast tissue at 1064 nm. Photograph of the (a) agar gel phantom containing PIGD NPs dots with different concentrations (s1 to s3: 1.0, 0.5, and 0.25 mg/mL, respectively), (b) stack of chicken tissue layers on the agar phantom, (c–g) PA images of the agar gel phantom containing PIGD NPs solutions acquired at different depths, (h) SNR with different PIGD NPs concentration as a function of penetration depth inside chicken-breast tissue. Laser energy density used on tissue surface is ~25 mJ/cm^2.

displayed a broad absorption band, mainly covering the range from 800 to 1200 nm [Fig. 1(e)] with a maximum ($\lambda_{abs,max}$) at 960 nm. The presentation of the absorption spectrum of PIGD in toluene, in comparison with its colloidal nanoparticle in water, is to understand the aggregation of PIGD inside the core of the nanoparticles. As compared with that of PIGD in dilute toluene ($\lambda_{abs,max} = 1100$ nm), a significant blue shift of absorption band was observed. This behavior could be attributed to the formation of H-aggregates of PIGD macromolecules due to their high planarity and strong $\pi - \pi$ stacking in the aggregating state.[47] The measured absorption coefficient of the PIGD SNPs (40 μg/mL) at 1064 nm is ~1.5 cm^{-1}. The absorption coefficients of 40 μg/mL SNPs at 1064 nm reported are ~1.96 cm^{-1},[23] 2.2 cm^{-1},[22] and that for 0.5 mM copper sulfide is 1.5 cm^{-1}.[17]

3.2 *PA Signals from Blood and PIGD Samples at 1064 nm*

The strong light absorption of PIGD NPs in the second NIR region [Fig. 1(e)] suggests that the potential of these NPs as a second window contrast agent. To determine the suitable concentration of NPs for deep-tissue and *in vivo* imaging, the PA signals of PIGD were compared with the signal of rat blood at 1064 nm. The PA signal amplitude from 2 mg/mL PIGD NPs is ~10 times stronger than that from the blood. Figure 2(b) shows the PA signals from rat blood and PIGD NPs with 0.5, 1.0, and 2 mg/mL concentrations. Figure 2(c) shows that the PA signal intensities increased linearly with the concentration of PIGD NPs.

3.3 *Deep-Tissue Photoacoustic Imaging at 1064 nm*

To validate the advantage of PIGD for PA imaging in the NIR II window, deep-tissue imaging was conducted using the system shown in Fig. 2(a). The solutions of PIGD NPs with three different concentrations were embedded in an agar gel phantom [Fig. 3(a)]. The concentrations of three spots, s1, s2, and s3 are 1.0, 0.5, and 0.25 mg/mL, respectively. The phantom was placed under chicken-breast tissues with different thicknesses [Fig. 3(b)]. PA cross-sectional images were acquired with laser energy density ~25 mJ/cm^2 on the tissue surface. PA images at different depths are shown in Figs. 3(c)–3(g). The PA signals from all three spots (s1 to s3) detectable at the tissue depth up to 5 cm [Fig. 3(g)]. The signal-to-noise ratio (SNR) of these images were calculated using the relation, SNR (dB) $= 20 \times \log_{10}(\frac{V}{n})$, where V is the average of PA signal amplitudes, and n is the average of background noise amplitude. Figure 3(h) shows that with decreased NPs concentration, the

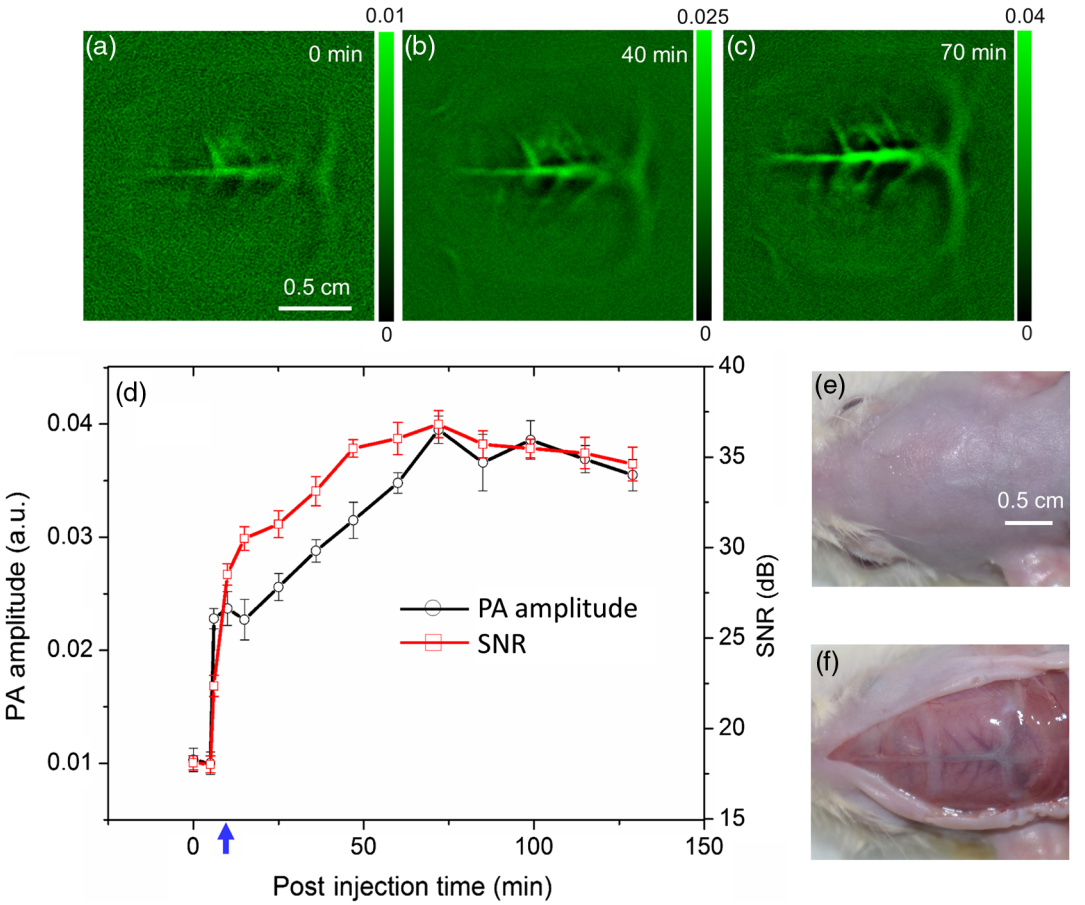

Fig. 4 *In vivo* PA imaging of rat brain vasculature: cross-sectional brain vascular images at (a) 0 min (before injection), (b) 40 min-, (c) 70 min postinjection of PIGD NPs. PIGD NP solution (2 mg/mL) was administered via tail vein injection with a dose of 0.25 mL per 100-gm body weight, (d) PA amplitude and SNR (dB) as a function of postinjection time. The blue arrow indicates injection point. Photograph of rat brain before (a) and after (b) removing the scalp. Laser energy density used for brain vascular imaging is ~5 mJ/cm^2.

SNR gradually decreased. The decrease in SNR is due to the fact that the 1064 nm beam was weakened as the depth of the chicken-breast tissue increased due to the light scattering and absorption by tissue. According to ANSI safety limit, the maximum permissible exposure (MPE) for skin is 100 mJ/cm^2 for 1064-nm laser.[16] Due to the limitation of laser power, we could use 25 mJ/cm^2 for deep-tissue imaging. But additional improvement in imaging depth can be achieved using higher energy lasers. These deep imaging results demonstrated that PIGD NPs could act as an excellent PAT agent to enhance the PA contrast for potential use in noninvasive deep-tissue imaging.

3.4 *In Vivo Brain Vascular Imaging on Rats at 1064 nm*

To evaluate the PA imaging capability of PIGD NPs, *in vivo* imaging of rat brain was performed. PAT imaging was done noninvasively, i.e., with skin and skull intact. As shown in Fig. 4, the cerebral cortex of a rat was imaged by PAT system [Fig. 2(a)] at 1064 nm before and after a single injection of PIGD NPs (0.25 mL per rat, 2 mg/mL). The cross-sectional images of the rat brain before injecting NPs are shown in Fig. 4(a). Although the brain vasculature is visible, the contrast of the image is poor due to little absorption of blood at 1064 nm. The SNR of this image is ~18 dB. After intravenous injection of PIGD NPs (0.25 mL per rat, 2 mg/mL), the PA signals from the blood vessels were increased. Brain vascular images were collected for about 2 h after injection. From the postinjection images, we observed that compared with the vascular image based on intrinsic contrast agent [Fig. 4(a)], the images acquired after the administration of NPs show the brain vasculature with better contrast. The NPs circulating in the blood stream enhanced the contrast between the blood vessels and the brain parenchyma, showing the ability of PIGD NPs to generate strong PA signal. Brain cortex images of the rat acquired at 40- and 70-min postinjection time are shown in Figs. 4(b) and 4(c), respectively. The SNR of these images is ~29 and ~37 dB, respectively. Figure 4(d) shows the PA signal in the blood vessel area and image SNR as a function of postinjection time. From the graph, it is clear that the PIGD in the blood vessels helped to enhance the PA contrast. After injecting the NPs in to the blood stream, the concentration of NPs increased within the cortex vessels and reached maximum ~70 min as shown in Fig. 4(d). The SNR of the image collected at 70 min is ~2 times higher than that of image collected at 0 min (preinjection image). The increase SNR achieved after the injection of NPs indicates that PIGD NPs could act as an excellent PA contrast agent. After 70-min postinjection, the PA signal remained strong, indicating a sufficient number of NPs circulating in the blood. The NPs circulation was monitored for a relatively short period (~120 min). But, the actual circulation time of the NPs in the vasculature could be longer. Long-circulation of NPs could be due to their suitable size of ~25 nm and the PEGylated surfaces of the NPs. The photographs of the brain taken before and after opening the scalp are shown in Figs. 4(e) and 4(f), respectively. An open scalp anatomical photograph of the cortex vasculature was taken after removing the scalp for comparison. This *in vivo* brain studies proved that the distribution of long-circulating NPs in the vasculature can provide contrast-enhanced PA imaging of brain vessels of rats with intact skin and skull.

4 Conclusions

We have demonstrated deep-tissue and contrast-enhanced *in vivo* photoacoustic imaging in NIR-II window using a new type of SPNs as an exogenous contrast agent. An imaging depth of ~5 cm was achieved at 1064 nm with an excitation laser energy density of 25 mJ/cm^2. The contrast of the brain vasculature was enhanced by ~2 times, 70 min after the injection of PIGD NPs (0.25 mL, 2 mg/mL) in living rats. The energy density used for *in vivo* imaging was 5 mJ/cm^2. The imaging depth and contrast of brain vasculature could be further enhanced by increasing the excitation energy density, e.g., up to 100 mJ/cm^2 for 1064 nm imaging. Although the SNPs in the present work were imaged at 1064 nm, they can serve as a PA contrast agent also in the wavelength range of 750 to 1100 nm [Fig. 1(e)]. Thus, PIGD SNPs as an efficient NIR-II PA contrast agent opens new opportunities for biomedical imaging with enhanced contrast and depth.

Disclosures

Authors have no relevant financial interests in this work and no other potential conflicts of interest to disclose.

Acknowledgments

M.P. is grateful to the financial support from the Singapore Ministry of Health's National Medical Research Council (NMRC/OFIRG/0005/2016: M4062012). M.W. is grateful to the funding support by a start-up grant of Nanyang Assistant Professorship (M4080992) from Nanyang Technological University, and AcRF Tier 2 (ARC 36/13: M4020172) from the Ministry of Education, Singapore.

References

1. L. Li et al., "Single-impulse panoramic photoacoustic computed tomography of small-animal whole-body dynamics at high spatiotemporal resolution," *Nat. Biomed. Eng.* **1**, 0071 (2017).
2. P. K. Upputuri and M. Pramanik, "Recent advances toward preclinical and clinical translation of photoacoustic tomography: a review," *J. Biomed. Opt.* **22**(4), 041006 (2017).
3. L. V. Wang and J. Yao, "A practical guide to photoacoustic tomography in the life sciences," *Nat. Methods* **13**(8), 627–638 (2016).
4. A. Taruttis and V. Ntziachristos, "Advances in real-time multispectral optoacoustic imaging and its applications," *Nat. Photonics* **9**(4), 219–227 (2015).
5. L. V. Wang and S. Hu, "Photoacoustic tomography: in vivo imaging from organelles to organs," *Science* **335**(6075), 1458–1462 (2012).
6. Q. Chen et al., "A self-assembled albumin-based nanoprobe for in vivo ratiometric photoacoustic pH imaging," *Adv. Mater.* **27**(43), 6820–6827 (2015).
7. P. K. Upputuri and M. Pramanik, "Performance characterization of low-cost, high-speed, portable pulsed laser diode photoacoustic tomography (PLD-PAT) system," *Biomed. Opt. Express* **6**(10), 4118–4129 (2015).
8. S. Huang et al., "A dual-functional benzobisthiadiazole derivative as an effective theranostic agent for near-infrared photoacoustic imaging and photothermal therapy," *J. Mater. Chem. B* **4**(9), 1696–1703 (2016).
9. C. Kim, C. Favazza, and L. V. Wang, "In vivo photoacoustic tomography of chemicals: high-resolution functional and molecular optical imaging at new depths," *Chem. Rev.* **110**(5), 2756–2782 (2010).
10. M. Pramanik et al., "Single-walled carbon nanotubes as a multimodal-thermoacoustic and photoacoustic-contrast agent," *J. Biomed. Opt.* **14**(3), 034018 (2009).
11. K. Sivasubramanian et al., "Near Infrared light-responsive liposomal contrast agent for photoacoustic imaging and drug release applications," *J. Biomed. Opt.* **22**(4), 041007 (2017).

12. Y. Shi et al., "Targeted Aucore–Agshell nanorods as a dual-functional contrast agent for photoacoustic imaging and photothermal therapy," *Biomed. Opt. Express* **7**(5), 1830–1841 (2016).
13. J. R. Rajian et al., "Drug delivery monitoring by photoacoustic tomography with an ICG encapsulated double emulsion," *Opt. Express* **19**(15), 14335–14347 (2011).
14. S. Zhu et al., "Molecular imaging of biological systems with a clickable dye in the broad 800- to 1, 700-nm near-infrared window," *Proc. Natl. Acad. Sci. U. S. A.* **114**(5), 962–967 (2017).
15. A. L. Antaris et al., "A small-molecule dye for NIR-II imaging," *Nat. Mater.* **15**(2), 235–242 (2016).
16. Laser Institute of America, "American National Standard for Safe Use of Lasers," *ANSI Standard Z136.1-2007*, New York (2007).
17. G. Ku et al., "Copper sulfide nanoparticles as a new class of photoacoustic contrast agent for deep tissue imaging at 1064 nm," *ACS Nano* **6**(8), 7489–7496 (2012).
18. K. Homan et al., "Prospects of molecular photoacoustic imaging at 1064 nm wavelength," *Opt. Lett.* **35**(15), 2663–2665 (2010).
19. Y. S. Chen et al., "Feasibility of contrast-enhanced photoacoustic liver imaging at a wavelength of 1064 nm," in *Biomedical Optics and 3D Imaging OSA*, OSA, Miami, Florida (2012).
20. Y. Zhou et al., "A phosphorus phthalocyanine formulation with intense absorbance at 1000 nm for deep optical imaging," *Theranostics* **6**(5), 688–697 (2016).
21. J. Zhou et al., "Compact plasmonic blackbody for cancer theranosis in near-infrared II window," *ACS Nano* **12**(3), 2643–2651 (2018).
22. Y. Jiang et al., "Broadband absorbing semiconducting polymer nanoparticles for photoacoustic imaging in second near-infrared window," *Nano Lett.* **17**(8), 4964–4969 (2017).
23. J. Wu et al., "Semiconducting polymer nanoparticles for centimeters-deep photoacoustic imaging in the second near-infrared window," *Adv. Mater.* **29**(41), 1703403 (2017).
24. K. Pu et al., "Semiconducting polymer nanoparticles as photoacoustic molecular imaging probes in living mice," *Nat. Nanotechnol.* **9**(3), 233–239 (2014).
25. B. Guo et al., "Biocompatible conjugated polymer nanoparticles for highly efficient photoacoustic imaging of orthotopic brain tumors in the second near-infrared window," *Mater. Horiz.* **4**(5), 1151–1156 (2017).
26. X. Deán-Ben et al., "Advanced optoacoustic methods for multiscale imaging of in vivo dynamics," *Chem. Soc. Rev.* **46**(8), 2158–2198 (2017).
27. H. Liu et al., "Multifunctional polymeric micelles loaded with doxorubicin and poly(dithienyl-diketopyrrolopyrrole) for near-infrared light-controlled chemo-phototherapy of cancer cells," *Colloids Surf. B, Biointerfaces* **157**, 398-406 (2017).
28. J. Weber, P. C. Beard, and S. E. Bohndiek, "Contrast agents for molecular photoacoustic imaging," *Nat. Methods* **13**(8), 639–650 (2016).
29. J. Liu et al., "Conjugated polymer nanoparticles for photoacoustic vascular imaging," *Polym. Chem.* **5**(8), 2854–2862 (2014).
30. A. R. Han et al., "ε-branched flexible side chain substituted diketopyrrolopyrrole-containing polymers designed for high hole and electron mobilities," *Adv. Funct. Mater.* **25**(2), 247–254 (2015).
31. G. K. Dutta et al., "Visible-near infrared absorbing polymers containing thienoisoindigo and electron-rich units for organic transistors with tunable polarity," *Adv. Funct. Mater.* **23**(42), 5317–5325 (2013).
32. C. B. Nielsen, M. Turbiez, and I. McCulloch, "Recent advances in the development of semiconducting DPP-containing polymers for transistor applications," *Adv. Mater.* **25**(13), 1859–1880 (2013).
33. Y. Ji et al., "Asymmetric diketopyrrolopyrrole conjugated polymers for field-effect transistors and polymer solar cells processed from a non-chlorinated solvent," *Adv. Mater.* **28**(5), 943–950 (2016).
34. R. Stalder, J. Mei, and J. R. Reynolds, "Isoindigo-based donor-acceptor conjugated polymers," *Macromolecules* **43**(20), 8348–8352 (2010).
35. I. Kang et al., "Effect of selenophene in a DPP copolymer incorporating a vinyl group for high-performance organic field-effect transistors," *Adv. Mater.* **25**(4), 524–528 (2013).
36. H. Chen et al., "Highly pi-extended copolymers with diketopyrrolopyrrole moieties for high-performance field-effect transistors," *Adv. Mater.* **24**(34), 4618–4622 (2012).
37. K. Wang et al., "Direct arylation polymerization toward ultra-low bandgap poly(thienoisoindigo-alt-diketopyrrolepyrrole) conjugated polymers: The effect of β-protection on the polymerization and properties of the polymers," *J. Polym. Sci. Part A: Polym. Chem.* **55**(19), 3205–3213 (2017).
38. S. K. Kalva and M. Pramanik, "Experimental validation of tangential resolution improvement in photoacoustic tomography using a modified delay-and-sum reconstruction algorithm," *J. Biomed. Opt.* **21**(8), 086011 (2016).
39. M. Pramanik, "Improving tangential resolution with a modified delay-and-sum reconstruction algorithm in photoacoustic and thermoacoustic tomography," *J. Opt. Soc. Am. A* **31**(3), 621–627 (2014).
40. H. Bohra and M. F. Wang, "Direct C-H arylation: a "Greener" approach towards facile synthesis of organic semiconducting molecules and polymers," *J Mater. Chem. A* **5**(23), 11550–11571 (2017).
41. J. Yao et al., "High-speed label-free functional photoacoustic microscopy of mouse brain in action," *Nat Methods* **12**(5), 407–410 (2015).
42. X. Wang and M. Wang, "Synthesis of donor-acceptor conjugated polymers based on benzo[1, 2-b:4, 5-b′]dithiophene and 2, 1, 3-benzothiadiazole via direct arylation polycondensation: towards efficient C-H activation in nonpolar solvents," *Polym. Chem.* **5**(19), 5784–5792 (2014).
43. G. Kim et al., "A thienoisoindigo-naphthalene polymer with ultrahigh mobility of 14.4 cm(2)/V.s that substantially exceeds benchmark values for amorphous silicon semiconductors," *J. Am. Chem. Soc.* **136**(26), 9477–9483 (2014).
44. I. Kang et al., "Record high hole mobility in polymer semiconductors via side-chain engineering," *J. Am. Chem. Soc.* **135**(40), 14896–14899 (2013).
45. C. Yang et al., "Robust Colloidal nanoparticles of pyrrolopyrrole cyanine J-aggregates with bright near-infrared fluorescence in aqueous media: from spectral tailoring to bioimaging applications," *Chemistry* **23**(18), 4310–4319 (2017).
46. C. Yang et al., "Hydrophobic-sheath segregated macromolecular fluorophores: colloidal nanoparticles of polycaprolactone-grafted conjugated polymers with bright far-red/near-infrared emission for biological imaging," *Biomacromolecules* **17**(5), 1673–1683 (2016).
47. R. Noriega et al., "A general relationship between disorder, aggregation and charge transport in conjugated polymers," *Nat. Mater.* **12**(11), 1038–1044 (2013).

Paul Kumar Upputuri received his PhD in physics from the Indian Institute of Technology (IIT), Madras, in 2010. Currently, he is working as a research fellow at the Nanyang Technological University. He has published around 80 papers in journals and conference proceedings. His research areas are optics, biomedical imaging, coherent Raman microscopy, ultrafast lasers, and optical instrumentation. He is a member of SPIE, OSA, Indian Laser Association (ILA), and Optical Society of India (OSI).

Mingfeng Wang received his PhD in polymer chemistry and materials in 2009 from the University of Toronto. Currently, he is a Nanyang assistant professor in the School of Chemical and Biomedical Engineering at Nanyang Technological University, Singapore. His current research focuses on synthetic chemistry of pi-conjugated semiconducting molecules and polymers, polymeric materials with bioinspired structures and advanced functions for optoelectronic and biomedical applications.

Manojit Pramanik received his PhD in biomedical engineering from Washington University in St. Louis, Missouri, USA. Currently, he is an assistant professor of the School of Chemical and Biomedical Engineering, Nanyang Technological University, Singapore. His research interests include the development of photoacoustic/thermoacoustic imaging systems, image reconstruction methods, clinical application areas, such as breast cancer imaging, molecular imaging, contrast agent development, and Monte Carlo simulation of light propagation in biological tissue.

Biographies for the other authors are not available.